Two energy scales of spin dimers in clinoclase $Cu_3(AsO_4)(OH)_3$

Stefan Lebernegg,[1] Alexander A. Tsirlin,[1,2,*] Oleg Janson,[1,2] and Helge Rosner[1,†]
[1]*Max Planck Institute for Chemical Physics of Solids, Nöthnitzer Strasse 40, 01187 Dresden, Germany*
[2]*National Institute of Chemical Physics and Biophysics, 12618 Tallinn, Estonia*
(Received 15 April 2013; published 13 June 2013)

Magnetic susceptibility measurements and a microscopic magnetic model of the mineral clinoclase $Cu_3(AsO_4)(OH)_3$ are reported. This spin-1/2 material can be well described as a combination of two nonequivalent spin dimers with the sizable magnetic couplings of $J \simeq 700$ K and $J_{D2} \simeq 300$ K but only small interdimer couplings. Based on density functional theory calculations, we pinpoint the location of dimers in the rather complex crystal structure. Counterintuitively, the largest exchange coupling operates between the structural Cu_2O_6 dimers. Additionally, we investigate magnetostructural correlations in Cu_2O_6 structural dimers by considering the influence of the hydrogen position on the magnetic coupling. To evaluate accurate exchange couplings, we establish the hydrogen positions that were not known so far and analyze the pattern of hydrogen bonding.

DOI: 10.1103/PhysRevB.87.235117 PACS number(s): 75.30.Et, 75.50.Ee, 75.10.Jm, 91.60.Pn

I. INTRODUCTION

The majority of magnetic systems have more than one characteristic energy scale, according to the different nature of interactions between the spins. For example, in low-dimensional magnets strong interactions within chains or planes are of direct exchange or superexchange type, whereas weak interchain (interplane) couplings may have purely dipolar origin.[1–3] The different energy scales of these interactions imply that, at sufficiently high temperatures, the magnetic behavior is solely determined by the strong couplings and the system can be fully described in terms of a low-dimensional spin model.[1,4] However, at low temperatures, interchain (interplane) couplings come into play, and a full three-dimensional description is required.

In complex spin systems, the identification of different energy scales is by no means a simple problem. Naively, one could think that distinct crystallographic positions of magnetic atoms should lead to different strengths of magnetic couplings and therefore to different energy scales of the magnetic behavior. Indeed, in spin-dimer systems, such as $BaCuSi_2O_6$ and NH_4CuCl_3, the spin-$\frac{1}{2}$ Cu^{2+} ions occupy several nonequivalent positions[5,6] and form different types of spin dimers which have a large impact on the high-field behavior, including the unusual critical regime of the Bose-Einstein condensation of magnons in $BaCuSi_2O_6$ (Ref. 7) and the fractional magnetization plateaus in NH_4CuCl_3 (Refs. 8 and 9). However, spin dimers can also be formed between two nonequivalent Cu positions, thus leading to only one type of spin dimer and one energy scale, as in the spin-ladder compound $BiCu_2PO_6$.[10]

When the system contains several Cu^{2+} positions with dissimilar local environments and variable connectivity of the Cu polyhedra, the identification of the relevant interactions and energy scales becomes increasingly complex. The problem of magnetic dimers that do not match structural dimers,[11–13] as well as magnetic chains running perpendicular to the structural chains,[14] is well known in quantum magnets and requires a careful microscopic analysis.

Here, we report on the magnetic behavior and microscopic modeling of clinoclase, $Cu_3(AsO_4)(OH)_3$. The intricate crystal structure of this mineral[15,16] features three nonequivalent Cu positions. Nevertheless, the resulting spin lattice comprises only two types of magnetic dimers with notably different interaction energies. Our microscopic analysis shows that one spin dimer is formed between two different Cu positions (Cu1-Cu2) and does not match the respective structural dimer. However, the other spin dimer coincides with the Cu3-Cu3 structural dimer. We argue that neither a straightforward comparison of Cu-Cu distances nor the application of the Goodenough-Kanamori-Anderson (GKA) rules for the superexchange[17–19] leads to the correct assignment of magnetic couplings in clinoclase. Therefore all geometrical details of relevant exchange pathways should be taken into account and considered simultaneously. We elaborate on this problem by determining the positions of hydrogen atoms and analyzing their role in the superexchange.

The outline of this paper is as follows. Section II summarizes experimental and computational techniques that were applied in this study. In Sec. III A, we report details of the sample characterization followed by the determination of hydrogen positions and the discussion of the crystal structure in Sec. III B. Section III C presents experimental magnetic properties and a brief discussion of them in terms of a phenomenological model of two spin dimers with different energy scales, and Sec. III D provides microscopic insight into this model and into residual interactions between the spin dimers. Finally, Sec. III E clarifies the role of hydrogen atoms in the Cu-O-Cu superexchange. Our work is concluded with a discussion and summary in Sec. IV.

II. METHODS

For our experimental studies, we used a natural sample of clinoclase from Wheal Gorland, St. Day United Mines (Cornwall, United Kingdom), which is the type locality of this rare mineral. The sample from the mineralogical collection of Salzburg University (Department of Materials Engineering and Physics) features bulky dark blue crystals of clinoclase together with smaller light blue crystals of liroconite, $Cu_2Al(AsO_4)(OH)_4{\cdot}4(H_2O)$. The crystals of clinoclase were manually separated from foreign phases and carefully analyzed by powder x-ray diffraction (XRD) and chemical analysis. Laboratory powder XRD data were collected using a Huber

G670 Guinier camera (CuKα_1 radiation, ImagePlate detector, $2\theta = 3^\circ$–100° angle range). Additionally, high-resolution XRD data were collected at the ID31 beam line of the European Synchrotron Radiation Facility (ESRF, Grenoble) at a wavelength of about 0.43 Å. The chemical composition was determined by the inductively coupled plasma optical emission spectrometry (ICP-OES) method.[20] The thermal stability of clinoclase was investigated by thermogravimetric analysis[21] up to 500 °C.

The magnetic susceptibility of clinoclase was measured with a Quantum Design MPMS superconducting quantum interference device (SQUID) magnetometer in the temperature range of 2–380 K in fields up to 5 T.

Electronic structure calculations were performed within the density functional theory (DFT) by using the full-potential local-orbital code FPLO9.07-41.[22] Local-density approximation (LDA)[23] and generalized gradient approximation (GGA)[24] were used for the exchange-correlation potential, together with a well converged k mesh of $6 \times 6 \times 6$ points for the crystallographic unit cell of clinoclase and about 100 points in supercells. Hydrogen positions missing in the presently available crystallographic data[15,16] were obtained by structural optimizations with a threshold for residual forces of 2 meV/Å.

The effects of strong electronic correlations, typical for cuprates, were considered by mapping the LDA bands onto an effective tight-binding (TB) model. The transfer integrals t_i of the TB model are evaluated as nondiagonal matrix elements in the basis of Wannier functions (WFs). These transfer integrals t_i are further introduced into the half-filled, effective one-orbital Hubbard model $\hat{H} = \hat{H}_{TB} + U_{\rm eff} \sum_i \hat{n}_{i\uparrow}\hat{n}_{i\downarrow}$ that is eventually reduced to the Heisenberg model for the low-energy excitations,

$$\hat{H} = \sum_{\langle ij \rangle} J_{ij} \hat{S}_i \cdot \hat{S}_j, \qquad (1)$$

where the summation is done over bonds $\langle ij \rangle$. For the half-filled case, which applies to clinoclase, the reduction to the Heisenberg model is well justified in the strongly correlated limit $t_i \ll U_{\rm eff}$, with the effective on-site Coulomb repulsion $U_{\rm eff}$ exceeding t_i by at least an order of magnitude (see Table II). This procedure yields the antiferromagnetic (AFM) contributions to the exchange coupling evaluated as $J_i^{\rm AFM} = 4t_i^2/U_{\rm eff}$. For $U_{\rm eff}$ we have chosen 4 eV.[25,26]

Alternatively, full exchange couplings J_i, comprising ferromagnetic (FM) and AFM contributions, can be derived from differences in total energies of various collinear spin arrangements, as evaluated in spin-polarized supercell calculations within the density functional theory local spin-density approximation (LSDA) + U formalism that includes a static mean-field correction for correlation effects. An "around-mean-field" (AMF) and a "fully localized limit" (FLL) approximation for correcting the double counting were used.[27] Both types supplied consistent results, so only the AMF results are presented here. The on-site Coulomb repulsion and on-site Hund's exchange of the Cu $3d$ orbitals are chosen as $U_d = 6.5 \pm 0.5$ eV and $J_d = 1$ eV, respectively, according to the parameter set used for several other cuprates.[25,26,28]

In addition to periodic DFT calculations, we performed a series of cluster calculations that pinpoint the effect of hydrogen atoms on the superexchange. The cluster under consideration is based on a $Cu_2O_6H_5$ dimer embedded in a set of point charges, with two As ions bonded to the dimer considered as total ion potentials (TIPs).[29,30] The embedding was chosen so that the intradimer hopping obtained from the cluster and periodic LDA calculations match. The cluster calculations were done with the ORCA 2.9 code[31,32] in combination with a 6-311 ++ G(d, p) basis set and a Perdew Burke Ernzerhof zero (PBE0) hybrid functional.[33]

Quantum Monte Carlo (QMC) simulations were performed using the codes LOOP[34] and DIRLOOP_SSE[35] from the software package ALPS-1.3.[36] Magnetic susceptibility was simulated on finite lattices of $N = 2400$ spins $S = \frac{1}{2}$, using 40 000 sweeps for thermalization and 400 000 sweeps after thermalization. For simulations of magnetization isotherms, we used 4000 sweeps for thermalization and 40 000 sweeps after thermalization. Magnetization of the "2 + 1" model was simulated using the full diagonalization code from ALPS-1.3.[36]

III. RESULTS

A. Sample characterization

Powder XRD confirmed the purity of our clinoclase sample. However, the ICP-OES analysis showed slight deviations from the ideal composition: 49.6(3) wt % Cu, 18.3(1) wt % As compared to 50.1(1) wt % Cu, 19.7(1) wt % As expected for $Cu_3(AsO_4)(OH)_3$. Additionally, trace amounts of Ca and S (0.1–0.2 wt %) were found. Other detectable elements, including transition metals, are below 0.03 wt %.

To verify the composition of the clinoclase phase, we performed structure refinement using high-quality synchrotron data collected at room temperature. The lattice parameters we obtained for the space group $P2_1/c$ are $a = 7.266$ Å, $b = 6.459$ Å, $c = 12.393$ Å, with the monoclinic angle $\beta = 99.49^\circ$. They agree well with the existing single-crystal data,[16] where $a = 7.257$ Å, $b = 6.457$ Å, $c = 12.378$ Å, and $\beta = 99.51^\circ$, which we used for the magnetic modeling. Our refinement confirmed full occupation of all atomic positions in the clinoclase structure.[37] As Cu and As are the two heaviest elements (and therefore strongest scatterers) in $Cu_3(AsO_4)(OH)_3$, their content in the crystalline phase is safely established by XRD. Regarding the bulk composition, the slight deficiency of Cu and As, as revealed by chemical analysis, may be attributed to trace amounts of secondary phases, such as $CaCO_3$ and $CaSO_4$, that are possible impurities in natural samples. Another plausible impurity is CuO (tenorite), which is difficult to identify by XRD because its strongest reflections overlap with those of clinoclase. Note that none of the possible impurities reveal any conspicuous effects in the magnetic susceptibility and should not affect our experimental results reported in Sec. III C.

Thermogravimetric analysis (TGA) identified the onset of the decomposition at about 180 °C and the weight loss of 7.1 % upon heating to 500 °C.[37] This weight loss implies the release of 1.5 water molecules per formula unit, as expected for $Cu_3(AsO_4)(OH)_3$. The sample recovered after the heating contained a mixture of unknown phases. Their composition and crystal structures require further investigation that lies beyond the scope of the present study.

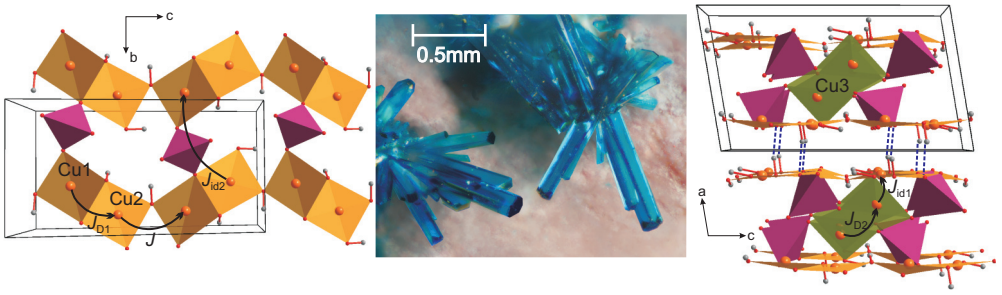

FIG. 1. (Color online) The crystal structure of clinoclase. The D1 (Cu1-Cu2) structural dimers are shown in orange, and the D2 (Cu3-Cu3) dimers are in green. The left panel shows a single layer consisting of zigzag chains of D1 dimers linked by AsO_4 tetrahedra (pink). In the right panel, the sandwich-like structure of clinoclase is visible with the hydrogen bonds shown as blue dashed lines. Arrows indicate the leading hopping pathways. The middle panel shows high-quality natural clinoclase crystals from the Majuba Hill Mine, Pershing County, Nevada, United States.

B. Crystal structure

Clinoclase crystallizes in the monoclinic space group $P2_1/c$ and forms a fairly complex crystal structure with three nonequivalent Cu positions (Fig. 1).[16] All Cu sites have a fivefold square-pyramidal coordination, where the four oxygen atoms in the basal plane form shorter bonds to Cu (1.9–2.1 Å), whereas the distance to the axial oxygen atom is above 2.3 Å. Similar to other cuprates, superexchange pathways and ensuing magnetic interactions can be described by resorting to the planar CuO_4 coordination because the oxygen atom in the axial position of the pyramid does not take part in the superexchange (see Sec. III D).

The CuO_4 plaquettes around the Cu1 and Cu2 sites form doubly bridged dimers (D1 = Cu1-Cu2) that share corners and build zigzag chains directed along [001]. The AsO_4 tetrahedra connect these chains into layers in the *bc* plane. Two layers of this type form a "sandwich" encompassing the dimers of Cu3 atoms (D2 = Cu3-Cu3). Although both D1 and D2 dimers are built of two CuO_4 plaquettes sharing a common edge, their symmetries and geometrical parameters are different. For example, the inversion symmetry in the center of D2 entails two equal Cu3-O-Cu3 angles. In contrast, D1 has no symmetry elements; hence its two Cu1-O-Cu2 bridging angles are not equal.

The connections between the "sandwiches" are restricted to hydrogen bonds and to long Cu-O bonds in the axial positions of the CuO_5 pyramids. This weak interlayer bonding is responsible for the perfect cleavage of clinoclase crystals parallel to (100) and for the low (Mohs) hardness of 2.5–3 in this material.[38]

Previous structure determinations[15,16] were based on XRD data and did not report the positions of hydrogen atoms. However, precise positions of all atoms, including hydrogen, are required for DFT band structure calculations and ensuing microscopic analysis of the electronic and magnetic structures. Therefore, we determined the hydrogen positions by relaxing the crystal structure of clinoclase. Only the hydrogen positions were optimized, whereas all other atoms were fixed to their experimental positions.[39] In the starting model, hydrogen atoms were attached to three out of seven oxygen atoms at a typical O-H distance of 1.0 Å. The orientation of the O-H bonds was random, although we made sure that the hydrogen atoms are well separated from other atoms in the clinoclase structure. While there is freedom in choosing three oxygen atoms forming covalent bonds to hydrogen, only those oxygen atoms that do not belong to the AsO_4 tetrahedra led to structures with low energies. When hydrogen atoms are attached to oxygen atoms belonging to the AsO_4 tetrahedra, the energy is much higher; hence such structures can be ruled out. This is in agreement with the empirical assignment of the OH groups in the experimental crystallographic study.[16]

The resulting hydrogen positions are listed in Table I. Further details of the relaxation procedure and comparisons to the experiment for other Cu^{2+} hydroxy salts can be found in Refs. 28 and 40. The optimized O-H distances are close to 1.0 Å, as expected for the covalent O-H bonds. Each hydrogen atom also forms one longer contact of about 1.8 Å (hydrogen bond) to another oxygen atom. Two of these contacts provide additional bonding within the layer,[37] whereas the hydrogen bond formed by H2 connects adjacent sandwiches (see Fig. 1). This arrangement of hydrogen bonds correlates with the positions of the hydrogen atoms: while H1 and H3 are nearly coplanar with Cu and O atoms, H2 is notably shifted along the *a* direction toward the neighboring sandwich. Therefore H1 and H3 lie in the plane of the D1 dimer plaquettes, whereas H2 and the respective O-H bond are in the out-of-plane position.

C. Magnetization measurements and phenomenological fits

The temperature dependence of the magnetic susceptibility $\chi(T)$ is shown in Fig. 2. In quantum magnets, $\chi(T)$ typically has an asymmetric domelike shape, with a broad maximum, indicating a gradual crossover from the high-temperature (paramagnetic) to the low-temperature (correlated) regime. Due to the unusually high magnetic energy scale in clinoclase, this maximum is shifted to high temperatures (~300 K) and

TABLE I. Hydrogen positions obtained by LDA/GGA structure optimization. The positions of oxygens forming short O-H bonds to these hydrogen atoms are given in parentheses.

atom	x/a	y/b	z/c
H1 (O5)	0.7429/0.7493	0.3513/0.3515	0.4799/0.4807
H2 (O6)	0.9362/0.9346	0.4685/0.4680	0.6792/0.6786
H3 (O7)	0.1522/0.1511	0.1635/0.1648	0.4876/0.4864

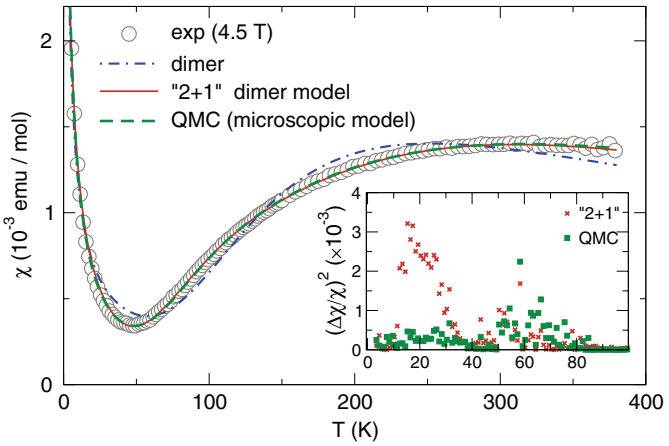

FIG. 2. (Color online) Experimental magnetic susceptibility (circles) of clinoclase $Cu_3(AsO_4)(OH)_3$ and fits using a dimer model (dash-dotted line), the phenomenological model [Eq. (3)] of $2+1$ dimers (solid line), and the microscopic model of coupled spin dimers, as shown in Fig. 8 (dashed line, QMC fit). Besides the intrinsic dimer susceptibility [Eq. (2)], we accounted for the temperature-independent contribution and a Curie-Weiss impurity and/or defect contribution. The inset shows difference curves for the $2+1$ dimer solution and the QMC fit.

is barely visible in the data collected below and around room temperature. Unfortunately, high-temperature measurements are not possible because the decomposition of clinoclase starts at about 450 K.[37]

The upturn in $\chi(T)$ below 50 K is a typical extrinsic feature caused by defects and/or impurities. It can be reasonably described by a Curie-Weiss law with $C_{\rm imp} = 0.015$ emu K/mol, corresponding to 3.2% of $S = \frac{1}{2}$ impurities per f.u., and $\theta_{\rm imp} = 2.5$ K. After subtraction of the extrinsic contribution, we obtain vanishingly small susceptibility below 30 K and an activated (exponential) behavior at higher temperatures, evidencing the gapped nature of the magnetic excitation spectrum.

The gap between the lowest-lying $S = 0$ and $S = 1$ states (the spin gap) is inherent to numerous magnetic models. The simplest one is a quantum-mechanical spin dimer with a singlet ground state. Indeed, the structure of clinoclase features well-defined structural dimers D1 and D2 that are evocative of the spin-dimer magnetism. For a system of isolated dimers, the magnetic susceptibility is given by the exact analytical expression:

$$\chi(T) = \frac{Ng^2\mu_{\rm B}^2}{T}\frac{1}{(3+\exp[J/T])}, \tag{2}$$

where J is the magnetic exchange within the dimer. The fit yields $J = 415$ K, but it does not account for the shape of the experimental curve, as shown in Fig. 2. Moreover, the resulting value of the g factor ($g = 1.48$) is unrealistically small for Cu^{2+}.

The failure of the isolated dimer model suggests that the magnetic couplings in clinoclase are more intricate. Prior to the microscopic evaluation (Sec. III D), we attempt to describe the $\chi(T)$ dependence with a phenomenological magnetic model. According to Sec. III B, the monoclinic unit cell of clinoclase contains three structural dimers formed by edge-sharing CuO_4 plaquettes (Fig. 1). Two of these dimers are of the D1 type (Cu1-Cu2), whereas the third dimer is D2 (Cu3-Cu3). Naturally, the magnetic couplings within D1 are different from those in D2. This brings us to a tentative model of $2+1$ dimers:

$$H = 2H_{\rm D1} + H_{\rm D2}, \tag{3a}$$

$$H_{\rm D1} = \frac{1}{2}\sum_{\substack{i\in{\rm Cu1}\\ j\in{\rm Cu2}}} J_{\rm D1}(\mathbf{S}_i\cdot\mathbf{S}_j), \tag{3b}$$

$$H_{\rm D2} = \sum_{\langle i,j\rangle\in{\rm Cu3}} J_{\rm D2}(\mathbf{S}_i\cdot\mathbf{S}_j), \tag{3c}$$

where $J_{\rm D1}$ and $J_{\rm D2}$ denote the magnetic couplings in the respective dimers. For each dimer, the magnetic susceptibility is given by Eq. (2).

Two scenarios are possible: either $J_{\rm D1} > J_{\rm D2}$ or vice versa. Fitting to the experimental curve readily shows that the $J_{\rm D2} > J_{\rm D1}$ solutions do not reproduce the experimental behavior. In contrast, the model with $J_{\rm D1} > J_{\rm D2}$ yields an excellent fit with $J_{\rm D1} = 703.5$ K, $J_{\rm D2} = 289.3$ K, and $g = 1.86$ (solid line in Fig. 2). Therefore, the smaller gap of ~290 K comes from the Cu3-Cu3 dimers (D2), while the Cu1-Cu2 dimers (D1) give rise to the larger gap of ~700 K.

D. Microscopic magnetic model

Now, we compare the above phenomenological model with the microscopic results based on DFT. In the first step, LDA calculations are performed. The width of the whole valence band block of about 9 eV is typical for cuprates (see Fig. 3). The spurious metallicity of the energy spectrum is a well-known shortcoming of LDA due to the underestimated electronic correlation in the Cu $3d$ shell.[41] Nevertheless, the LDA bands around the Fermi level (the energy range from −0.5 to 0.7 eV) are sufficient to describe low-energy magnetic excitations, provided that a suitable correlation part is added to the model Hamiltonian. The relevant bands are essentially of Cu d_{xy} character, with sizable contributions from O $2p$ orbitals. The orbital symmetry is defined with respect to the local coordinate system on each CuO_4 plaquette, where the Cu-Cu bond of the dimer is chosen as the local x axis, and the z axis is orthogonal to the plaquette plane. Note that this setting is different from the standard one, where x and y axes are directed along the Cu-O bonds, so that the highest crystal-field level has the $d_{x^2-y^2}$ symmetry.

The leading hopping parameters t_i and corresponding AFM exchanges $J_i^{\rm AFM} = 4t_i^2/U_{\rm eff}$ are listed in Table II. The results of the model analysis are supported by the evaluation of full exchange integrals J_i using total energies of collinear spin configurations calculated with LSDA + U. These two approaches are complementary. The model analysis provides information on all exchange couplings in the system and guides the LSDA + U calculations that are restricted to only a handful of leading interactions.

Our model analysis based on the hopping parameters t_i identifies five leading AFM exchanges that exceed 100 K (see $J_i^{\rm AFM}$ in Table II). The perfect agreement between the LDA bands at the Fermi level and those calculated with the Cu-centered Wannier functions (Fig. 3) confirms that the relevant

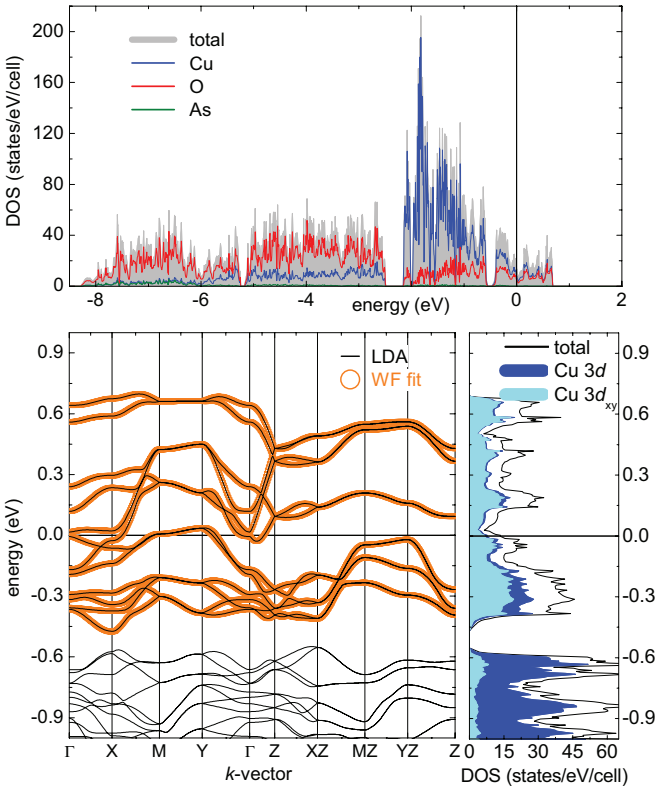

FIG. 3. (Color online) The LDA density of states (DOS) and the band structure of clinoclase $Cu_3(AsO_4)(OH)_3$. The top panel shows the contributions of the Cu($3d$), O($2p$), and As states to the total DOS. The Fermi level is at zero energy. In the bottom left panel, the LDA bands around the Fermi level are displayed and compared with bands derived from a fit using an effective one-band tight-binding model based on Cu-centered Wannier functions projected on local Cu($3d_{xy}$) orbitals. The k points are defined as follows: $\Gamma = (000)$, $X = (\frac{\pi}{a}00)$, $Y = (0\frac{\pi}{b}0)$, $Z = (00\frac{\pi}{c})$, $XZ = (\frac{\pi}{a}0\frac{\pi}{c})$, $MZ = (\frac{\pi}{a}\frac{\pi}{b}\frac{\pi}{c})$, $YZ = (0\frac{\pi}{b}\frac{\pi}{c})$. The bottom right panel shows that the partial Cu($3d$) DOS at the Fermi level is basically of Cu($3d_{xy}$) character, justifying our construction of the WFs.

superexchange pathways in clinoclase can be well described in terms of the CuO_4 plaquettes. Despite the short Cu-Cu distance of only 3.3 Å between the Cu atoms in two contiguous sandwiches along the a direction, the respective hopping is negligibly small (below 20 meV) because the magnetic orbitals lie in the bc plane and do not significantly overlap. Likewise,

TABLE II. Leading exchange couplings in clinoclase $Cu_3(AsO_4)(OH)_3$: Cu-Cu distances $d_{\text{Cu-Cu}}$ (in Å), bridging angles $\varphi_{\text{Cu-O-Cu}}$ (in degrees), hopping integrals t_i (in meV), and antiferromagnetic contributions $J_i^{\text{AFM}} = 4t^2/U_{\text{eff}}$ (in K) with $U_{\text{eff}} = 4.0$ eV. J_i (in K) are calculated with LSDA + U using $U_d = 6.5 \pm 0.5$ eV, $J_d = 1$ eV.

	$d_{\text{Cu-Cu}}$	$\varphi_{\text{Cu-O-Cu}}$	t_i	J_i^{AFM}	J_i
J_{D1}	2.98	93.6/99.9	−115	153	-4 ± 8
J_{D2}	3.13	101.9	191	423	302 ± 53
J_{id1}	3.38	124.6	−117	159	161 ± 25
J	3.66	149.3	276	884	693 ± 99
J_{id2}	5.52	–	−106	130	159 ± 31

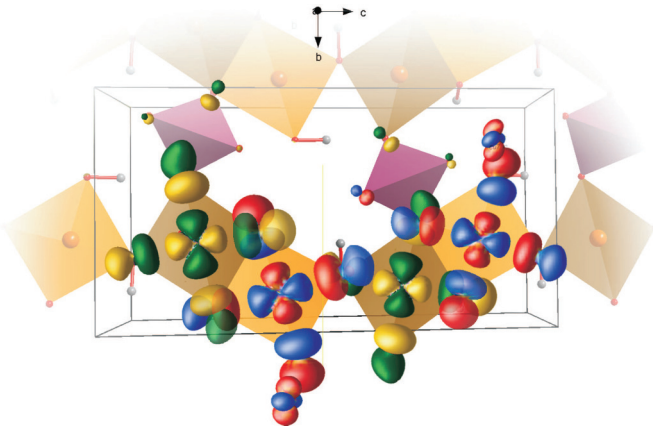

FIG. 4. (Color online) Wannier functions on the Cu1 (yellow-green) and Cu2 sites (red-blue). The net overlap at the two bridging oxygen atoms within the D1 dimers is significantly smaller than the overlap at the oxygen bridging two dimers. The Cu1 WF exhibits a considerable distortion towards the AsO_4 tetrahedra responsible for the large J_{id2} coupling.

two outer layers of each sandwich are coupled only via the Cu3 spins and lack any direct interaction.

The comparison between J_i^{AFM} and J_i in Table II shows that four out of five leading interactions are indeed AFM, with only small FM contributions. However, the coupling within D1 is nearly canceled because of comparable FM and AFM terms. The large FM contribution to J_{D1} ($J_{\text{D1}}^{\text{FM}} = J_{\text{D1}} - J_{\text{D1}}^{\text{AFM}} \simeq -160$ K) is indeed expected for the coupling geometry with bridging angles close to 90°.

Our microscopic model is consistent with the phenomenological analysis that suggested spin dimers with two different energy scales (Sec. III C). The coupling on D2 is $J_{\text{D2}} = 302$ K very close to 300 K found experimentally. However, the magnetic dimer with the coupling of about 700 K has to be reassigned. The coupling within D1 is in fact very weak, so that the spin dimer with $J \simeq 700$ K is formed not on the Cu1-Cu2 structural dimer D1 but between the respective dimers, where the CuO_4 plaquettes share a common corner instead of sharing a common edge (Figs. 4 and 5). This effect can be well understood in terms of the GKA rules for the superexchange and the overlap between neighboring Wannier functions (see Fig. 4) because the Cu-O-Cu angle for J is nearly 150° compared to only 93°–100° for J_{D1}. However, the GKA rules do not account for the fact that $J_{\text{D2}} \simeq 302$ K exceeds $J_{id1} \simeq 159$ K, even though the bridging angle for J_{D2} is notably smaller. This unusual behavior is further discussed in the next sections.

The reassignment of the magnetic dimer has no effect on the fit of the magnetic susceptibility presented in Sec. III C since it is independent of the position of the dimers in the crystal structure. The interdimer couplings J_{id1} and J_{id2} are nonfrustrated and can be taken into account by QMC. The resulting fit shown in Fig. 2 is only slightly better than the fit with the phenomenological 2 + 1 model. We find $J = 706.8$ K, $J_{\text{D2}} = 318.1$ K, and $g = 1.893$, in good agreement with our previous results. The main improvement is in the low-temperature region where the interdimer couplings become effective (see inset in Fig. 2). The couplings between

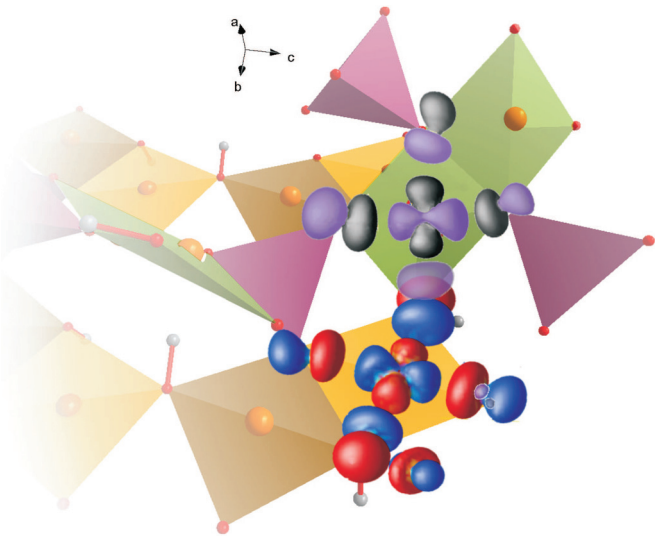

FIG. 5. (Color online) Wannier functions on the Cu2 (red-blue) and Cu3 (gray-violet). The overlap between Cu2 and Cu3 is hampered by the nonplanar arrangement of the CuO_4 plaquettes. The Cu3 WF features polarizations of the O($2p$) contributions caused by the AsO_4 tetrahedra.

the magnetic dimers were chosen as $J_{id1} = J_{id2} = 0.125\,J$ to yield the best agreement with the experimental curve.

E. Role of hydrogen

One important difference between the coupling pathways for J_{D1}, J_{D2}, and J_{id1} pertains to the positions of hydrogen atoms. While the bridging oxygen atoms of D2 belong to the AsO_4 tetrahedra and have only weak contacts to hydrogen, the bridging atom for J_{id1} and one of the bridging atoms of D1 form covalent O-H bonds. To study the role of the O-H bonds in more detail, we will focus on the D1 dimer, where, according to the very small exchange coupling and the planar Cu_2O_6 geometry, we expect interesting effects, e.g., a change from FM to AFM coupling.

The effect of the out-of-plane angle τ of the O-H bond on the intradimer coupling was studied by Ruiz *et al.*[42] for small organic ligands. They found that a large τ (out-of-plane position of hydrogen) favors FM coupling. We attempted to verify this effect for the D1 dimer in clinoclase. In a first step, the t_{D1} hopping parameters are calculated as a function of τ in the periodic model. The out-of-plane rotation of H up to 67°, which corresponds to the optimized crystal structure of clinoclase, reduces t_{D1} by about 40% and thus the AFM contribution to J_{D1} by about 60% (see the Supplemental Material).[37] Furthermore, t is slightly reduced, and the intersandwich hoppings decrease by about 50%. All other hoppings are more or less independent of τ.

For the calculation of J_{D1} as a function of τ, we used the $Cu_2O_6H_5$ cluster model, embedded in TIPs and point charges, which allows us to investigate the intradimer coupling exclusively. Additionally, the cluster enables us to vary the bridging angles without changing the whole set of additional structural parameters, which would be the case for a periodic model.[43]

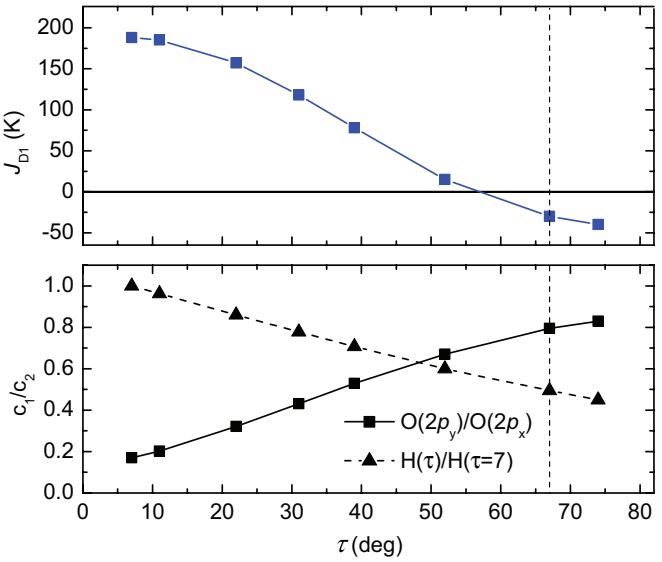

FIG. 6. (Color online) The top panel shows J_{D1} as a function of the out-of-plane angle of hydrogen τ. In the bottom panel, the ratio O($2p_y$)/O($2p_x$) of the WF contributions of the bridging oxygen bonded to H are displayed. The orbital character is denoted with respect to the coordinate system shown in Fig. 7. H(τ)/H($\tau = 7$) shows the H($1s$) contribution normalized to the value at $\tau = 7°$. The vertical dashed line indicates the computationally relaxed out-of-plane angle of hydrogen.

The results of the cluster calculations (Fig. 6) nicely show the transition from AFM to FM coupling upon an increase in τ. This effect is driven by the reduced hopping because the FM contribution $J_{D1}^{FM} = J_{D1} - J_{D1}^{AFM}$ is weakly dependent on τ and hovers around -150 K. The absolute size of J_{D1} obtained in the cluster calculations with the PBE0 functional is somewhat larger than the LSDA + U estimates. This is in fact not surprising because hybrid functionals, such as PBE0, tend to overestimate the exchange couplings.[30]

The decrease in t_{D1} can be traced back to the increasing contribution of the bridging oxygen O($2p_y$) to the WFs of the Cu1 and Cu2 sites (Fig. 6), while the O($2p_x$) contribution remains constant. At small τ, H($1s$) strongly interacts with O($2p_y$) and thus shifts its orbital energy downwards, which in turn reduces the interaction between this oxygen orbital and Cu($3d_{xy}$) orbitals. The H($1s$) contribution itself decreases with increasing τ. This is also visible in the WF picture (Fig. 7) as the rotation of the contribution of bridging oxygen atoms: As τ increases, the O($2p$) orbital turns into the direction perpendicular to the Cu-Cu axis of D1; hence the overlap of the WFs of Cu1 and Cu2, and thus the AFM part of the exchange, is reduced.

IV. DISCUSSION

The magnetism of clinoclase is well described by a model of two nonequivalent spin dimers. While this model is easily derived from the crystal structure of the mineral (Sec. III C), the arrangement of magnetic dimers cannot be established on purely empirical grounds. The two shortest Cu-Cu distances are formed within the structural dimers D1 and D2. Assuming that the magnetic coupling is more efficient at short distances,

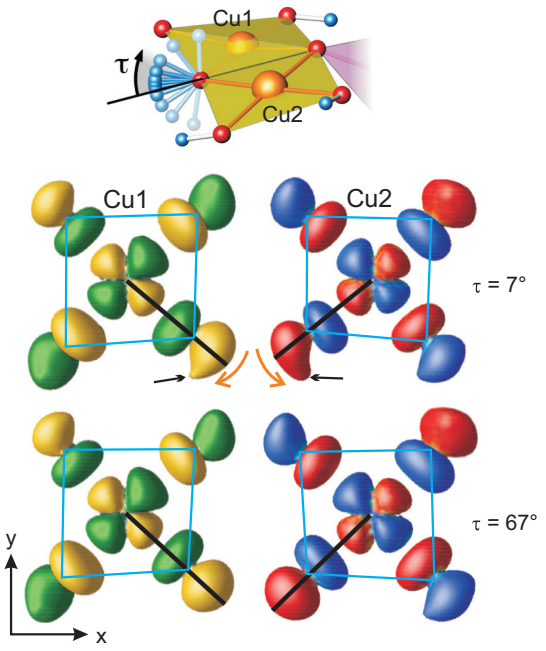

FIG. 7. (Color online) The effect of the out-of-plane rotation of hydrogen on the Wannier functions localized at the Cu1 and Cu2 sites. The top panel shows the D1 structural dimer with H, bonded to the bridging oxygen, being rotated out of the dimer plane by an angle τ. The middle and bottom panels show the WFs at the two Cu sites for $\tau = 7°$ and $\tau = 67°$, respectively. The CuO_4 plaquettes are indicated in light blue, and black lines connect the central Cu and the O bonded to H. With increasing τ, the O($2p$) orbital rotates (indicated by orange arrows) about a local z axis. This effect is visible with respect to the black line. Black arrows point at the H($1s$) contribution to the WFs. At $\tau = 67°$, which corresponds to the computationally relaxed structure, no such contributions are visible anymore.

one would identify these structural dimers as magnetic dimers. This assessment is correct for D2, yet it fails for D1, where the strong interaction J forming the magnetic dimer is found between the structural D1 dimers. The GKA rules could provide a more plausible scenario because they account for the fact that short Cu-Cu distances entail Cu-O-Cu angles close to 90° that are unfavorable for an AFM coupling. The reference to the GKA rules readily explains why the dimer is formed by J (bridging angle of 149.3°) and not by J_{D1} (bridging angles below 100°). However, a consistent application of these rules would also relegate the strength of J_{D2} that should be much smaller than J_{id1} according to the smaller Cu-O-Cu angle of 101.9° compared with 124.6° for the latter coupling.

In clinoclase, neither Cu-Cu distances nor Cu-O-Cu angles fully elucidate the microscopic scenario. To explain why J_{D2} exceeds J_{id1}, details of their superexchange pathways should be analyzed and compared. Apart from the hydrogen atoms considered in Sec. III E, we find two main differences between these couplings: (i) the number of bridging oxygen atoms, which is 2 for J_{D2} and 1 for J_{id1}, and (ii) the mutual arrangement of the CuO_4 plaquettes, which are coplanar for J_{D2} and strongly twisted for J_{id1}. Dividing the overall Cu-Cu hopping t_{D2} by 2, we obtain $t_{D2}^{\text{eff}} = 95$ meV, which reflects the transfer via a single Cu-O-Cu bridge (as in J_{id1}). This hopping is slightly below $|t_{id1}| = 117$ meV, but their difference is much smaller than expected for the bridging angles of 101.9° and 124.6°. For example, the model calculation from Ref. 44 suggests that t_{id1} should be at least twice as large as t_{D2}.

There are different scenarios explaining the large AFM coupling of J_{D2}: It may originate from the combined effect of the indirect Cu-O-Cu and direct Cu-Cu hoppings within the Cu_2O_6 structural dimer. While the Cu-O-Cu processes should be solely determined by the bridging angle, the direct hopping requires the coplanar arrangement of the CuO_4 plaquettes, which is the case only for J_{D2}. This explanation is in line with the robust AFM coupling observed in many other spin-dimer compounds, such as $TlCuCl_3$ (Ref. 45) and $SrCu_2(BO_3)_2$ (Ref. 46), despite their low bridging angles of 96°–98°. The same arguments could be applied to D1, where one of the bridging angles is as large as 100° and indeed leads to a sizable transfer $t_{D1} = -115$ meV. However, the out-of-plane O-H bond (see Sec. III E) has a strong impact on the superexchange and is responsible for the very weak coupling. This effect of side groups may also play an important role for D2, but in a different manner. Here, the bridging oxygen atoms belong to the AsO_4 tetrahedra that could amplify the AFM superexchange, similar to GeO_4 tetrahedra in $CuGeO_3$.[47] The reason for this effect is the polarization of bridging ligand orbitals due to the cation in the center of the anionic group. This polarization results in an increase of the overlap and thus of the hopping integral between the Wannier functions of the D2 dimer (Fig. 5). Note that the structural dimers in α-$Cu_2As_2O_7$ (bridging angle of 101.7°) are very similar to D2 and also feature a strong AFM coupling.[12,48]

Another interesting feature of clinoclase is the sizable interdimer coupling J_{id2}. In contrast to all magnetic couplings discussed so far, J_{id2} does not involve a direct connection between the CuO_4 plaquettes and occurs via the bridging AsO_4 tetrahedron. The efficiency of this superexchange pathway can be explained by the coplanar and moreover well-aligned arrangement of the CuO_4 plaquettes. Their positions are such that two Cu-O$\cdots$O-Cu contacts are formed. One of these contacts goes along the edge of the AsO_4 tetrahedron (see Fig. 4), while the second contact does not involve any bonds or polyhedra. Nevertheless, its short O$\cdots$O distance of 2.8–3.0 Å is likewise beneficial for the superexchange. The resulting coupling $J_{id2} \simeq 140$ K is comparable to the typical interaction via double PO_4 and AsO_4 bridges in $Sr_2Cu(PO_4)_2$,[49] $K_2CuP_2O_7$,[50] and $Cu_2As_2O_7$.[48]

Regarding the spin model of clinoclase, the "strong" (J) and "weak" (J_{D2}) magnetic dimers are joined into a planar structure (Fig. 8) by nonfrustrated interdimer couplings J_{id1} and J_{id2}. Three interpenetrating planes of this type together form one structural sandwich and remain nearly decoupled. Topologically, each of the three lattices represents a diluted square lattice of magnetic dimers, depicted schematically in Fig. 8.

This spin lattice only marginally differs from a simple superposition of two nonequivalent dimers. The phenomenological $2+1$ dimer model and the two-dimensional spin lattice provide nearly indistinguishable fits of the magnetic susceptibility (Fig. 2). The main difference occurs at low temperatures, where the interdimer couplings become effective. The field dependence of the magnetization, as calculated by QMC, is very close to the intuitive picture of isolated spin dimers (Fig. 9). The wide plateau at $M = \frac{1}{3}$ is

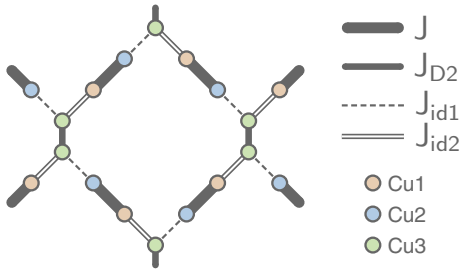

FIG. 8. (Color online) Microscopic magnetic model of clinoclase $Cu_3(AsO_4)(OH)_3$. Note that each structural sandwich depicted in Fig. 1 comprises three interpenetrating lattices of this type that are decoupled from each other. For the notation of magnetic couplings, see Table II.

due to the saturation of the weak dimers (J_{D2}), while the strong (J) dimers remain in the singlet state. Therefore, J_{id1} and J_{id2} have little effect on the magnetic susceptibility of clinoclase. Nevertheless, in many cases,[51] field-dependent magnetization measurements can provide complementary information to susceptibility data, especially when the latter suffer in their low-temperature part from defect or impurity contributions.

The effect of the weak interdimer couplings is visible by comparing the magnetization curves simulated for isolated dimers and for the dimers coupled by J_{id1} and J_{id2}, as shown in Fig. 8. In the model augmented by J_{id1} and J_{id2}, the transitions preceding and following the $\frac{1}{3}$ plateau are broadened compared to the $2+1$ dimer model (Fig. 9). This broadening is caused by the interdimer couplings J_{id1} and J_{id2} that give rise to a dispersion of magnetic excitations and mediate magnon-magnon interactions underlying the peculiar effect of spontaneous magnon decay.[52]

Clinoclase belongs to the family of gapped quantum magnets with nonequivalent spin dimers. In contrast to other systems of this type, different spin dimers are inherent to the crystal structure of this mineral. They are not formed due to a symmetry reduction upon a low-temperature phase transition that keeps similar magnetic interactions and therefore similar spin gaps in all dimers, as in $BaCuSi_2O_6$ (Ref. 5) and NH_4CuCl_3.[6] Clinoclase can be instead compared to

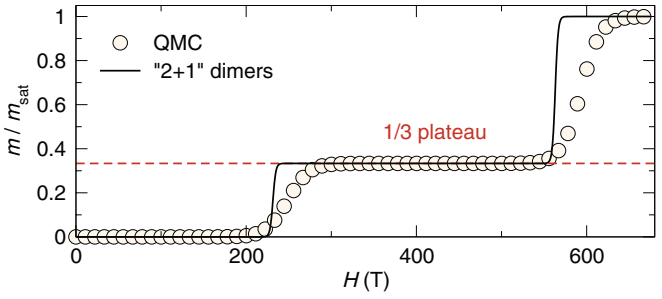

FIG. 9. (Color online) Magnetization isotherm of clinoclase $Cu_3(AsO_4)(OH)_3$ simulated using exact diagonalization of the $2+1$ dimers model and QMC for the microscopic magnetic model with $J : J_{D2} : J_{id1} : J_{id2} = 1 : 0.45 : 0.125 : 0.125$. The magnetic field is scaled adopting J and g values from the $\chi(T)$ fits (Fig. 2). m_{sat} is the saturation magnetization. Note two wide plateaus at $m/m_{sat} = 0$ and $m_{sat} = 1/3$.

the ambient-pressure modification of $(VO)_2P_2O_7$, where two distinct spin gaps of 32 and 65 K define two different energy scales of the system.[53–55] Systems of this type may show interesting high-field behavior because each group of dimers (J and J_{D2}) has independent low-temperature transitions related to the Bose-Einstein condensation (BEC) of magnons. The BEC transition takes place in the local field determined by the second group of dimers, either unpolarized J dimers for the BEC transition in J_{D2} or polarized J_{D2} dimers for the BEC transition in J. Unfortunately, the critical fields of clinoclase (Fig. 9) are too high to observe such effects using present-day high-field facilities. Nevertheless, the search for similar systems with structurally different spin dimers should be an interesting avenue to explore the high-field physics of quantum magnets.

V. SUMMARY

In summary, we performed a joint theoretical and experimental study of the magnetic behavior of the mineral clinoclase. Using density functional theory calculations, we evaluated the microscopic model for this compound and identified two types of spin dimers with the couplings $J \simeq 700$ K and $J_{D2} \simeq 300$ K. Intuitively, one is tempted to ascribe them to two types of structural Cu_2O_6 dimers in clinoclase. In fact, only J_{D2} pertains to the structural dimer D2, while the strong coupling J occurs between two corner-sharing D1 dimers. Additional couplings between the magnetic dimers reach 150 K but play a minor role in the magnetic behavior. Simulations for the DFT-based microscopic magnetic model yield excellent agreement with the experimental data.

The magnetic couplings in clinoclase are not solely determined by the Cu-O-Cu angles. The AsO_4 side groups and the hydrogen atoms also play an important role by enhancing or suppressing antiferromagnetic contributions to the short-range couplings J_{D1}, J_{D2}, and J_{id1}. Since no hydrogen positions were available from the experiment, we determined them by optimizing the crystal structure within DFT. We have demonstrated that the magnetic coupling within D1 is strongly affected by the hydrogen atom attached to one of the bridging oxygen atoms. The out-of-plane H position is responsible for the almost canceled exchange coupling J_{D1}. In turn, the strong dependence of the exchange couplings on the H positions and the excellent agreement of the DFT-derived microscopic magnetic model with the experimental data provide strong support for the reliability of the evaluated H positions. Our findings put forward details of the crystal structure, including inconspicuous and typically overlooked effects like hydrogen positions, as an important and even decisive factor in the magnetic superexchange.

ACKNOWLEDGMENTS

We are grateful to Gudrun Auffermann for her kind help with the chemical analysis. We also acknowledge the experimental support by Yurii Prots and Horst Borrmann (laboratory XRD) and Yves Watier (ID31) and the provision of the ID31 beam time by ESRF. We would like to thank the Department of Materials Engineering and Physics of the Salzburg University for providing the high-quality natural sample of clinoclase

from their mineralogical collection (inventory number 14797). A.T. and O.J. were supported by the European Union through the European Social Fund (Mobilitas Grants No. MTT77 and No. MJD447). S.L. acknowledges the funding from the Austrian Fonds zur Förderung der wissenschaftlichen Forschung (FWF) via a Schrödinger fellowship (J3247-N16).

*altsirlin@gmail.com
†helge.rosner@cpfs.mpg.de

[1] R. J. Birgeneau, H. J. Guggenheim, and G. Shirane, Phys. Rev. B **1**, 2211 (1970).
[2] A. Epstein, E. Gurewitz, J. Makovsky, and H. Shaked, Phys. Rev. B **2**, 3703 (1970).
[3] C. Zhou, D. P. Landau, and T. C. Schulthess, Phys. Rev. B **76**, 024433 (2007).
[4] H. M. Rønnow, D. F. McMorrow, and A. Harrison, Phys. Rev. Lett. **82**, 3152 (1999); P. A. Goddard, J. L. Manson, J. Singleton, I. Franke, T. Lancaster, A. J. Steele, S. J. Blundell, C. Baines, F. L. Pratt, R. D. McDonald, O. E. Ayala-Valenzuela, J. F. Corbey, H. I. Southerland, P. Sengupta, and J. A. Schlueter, *ibid.* **108**, 077208 (2012).
[5] D. V. Sheptyakov, V. Y. Pomjakushin, R. Stern, I. Heinmaa, H. Nakamura, and T. Kimura, Phys. Rev. B **86**, 014433 (2012); C. Rüegg, D. F. McMorrow, B. Normand, H. M. Rønnow, S. E. Sebastian, I. R. Fisher, C. D. Batista, S. N. Gvasaliya, C. Niedermayer, and J. Stahn, Phys. Rev. Lett. **98**, 017202 (2007); S. Krämer, R. Stern, M. Horvatić, C. Berthier, T. Kimura, and I. R. Fisher, Phys. Rev. B **76**, 100406(R) (2007).
[6] C. Rüegg, M. Oettli, J. Schefer, O. Zaharko, A. Furrer, H. Tanaka, K. W. Krämer, H.-U. Güdel, P. Vorderwisch, K. Habicht, T. Polinski, and M. Meissner, Phys. Rev. Lett. **93**, 037207 (2004).
[7] S. E. Sebastian, N. Harrison, C. D. Batista, L. Balicas, M. Jaime, P. A. Sharma, N. Kawashima, and I. R. Fisher, Nature (London) **441**, 617 (2006); O. Rösch and M. Vojta, Phys. Rev. B **76**, 224408 (2007); N. Laflorencie and F. Mila, Phys. Rev. Lett. **107**, 037203 (2011).
[8] W. Shiramura, K. Takatsu, B. Kurniawan, H. Tanaka, H. Uekusa, Y. Ohashi, K. Takizawa, H. Mitamura, and T. Goto, J. Phys. Soc. Jpn. **67**, 1548 (1998).
[9] H. Inoue, S. Tani, S. Hosoya, K. Inokuchi, T. Fujiwara, T. Saito, T. Suzuki, A. Oosawa, T. Goto, M. Fujisawa, H. Tanaka, T. Sasaki, S. Awaji, K. Watanabe, and N. Kobayashi, Phys. Rev. B **79**, 174418 (2009).
[10] B. Koteswararao, S. Salunke, A. V. Mahajan, I. Dasgupta, and J. Bobroff, Phys. Rev. B **76**, 052402 (2007); O. Mentré, E. Janod, P. Rabu, M. Hennion, F. Leclercq-Hugeux, J. Kang, C. Lee, M.-H. Whangbo, and S. Petit, *ibid.* **80**, 180413(R) (2009); A. A. Tsirlin, I. Rousochatzakis, D. Kasinathan, O. Janson, R. Nath, F. Weickert, C. Geibel, A. M. Läuchli, and H. Rosner, *ibid.* **82**, 144426 (2010).
[11] J. Deisenhofer, R. M. Eremina, A. Pimenov, T. Gavrilova, H. Berger, M. Johnsson, P. Lemmens, H.-A. Krug von Nidda, A. Loidl, K.-S. Lee, and M.-H. Whangbo, Phys. Rev. B **74**, 174421 (2006).
[12] O. Janson, A. A. Tsirlin, J. Sichelschmidt, Y. Skourski, F. Weickert, and H. Rosner, Phys. Rev. B **83**, 094435 (2011).
[13] M. Schmitt, A. A. Gippius, K. S. Okhotnikov, W. Schnelle, K. Koch, O. Janson, W. Liu, Y.-H. Huang, Y. Skourski, F. Weickert, M. Baenitz, and H. Rosner, Phys. Rev. B **81**, 104416 (2010).
[14] E. E. Kaul, H. Rosner, V. Yushankhai, J. Sichelschmidt, R. V. Shpanchenko, and C. Geibel, Phys. Rev. B **67**, 174417 (2003); A. A. Tsirlin and H. Rosner, *ibid.* **83**, 064415 (2011); O. Janson, A. A. Tsirlin, E. S. Osipova, P. S. Berdonosov, A. V. Olenev, V. A. Dolgikh, and H. Rosner, *ibid.* **83**, 144423 (2011).
[15] S. Ghose, M. Fehlmann, and M. Sundaralingam, Acta Crystallogr. **18**, 777 (1965).
[16] K. Eby and F. C. Hawthorne, Acta Cryst. C **46**, 2291 (1990).
[17] J. B. Goodenough, Phys. Rev. **100**, 564 (1955).
[18] J. Kanamori, J. Phys. Chem. Solids **10**, 87 (1959).
[19] P. W. Anderson, Solid State Phys. **14**, 99 (1963).
[20] ICP-OES analysis was performed with the Vista instrument from Varian.
[21] Measurements are done using a Netzsch STA 449C instrument with an Al_2O_3 crucible, argon gas, and a gas flow of 120 mL/min.
[22] K. Koepernik and H. Eschrig, Phys. Rev. B **59**, 1743 (1999).
[23] J. P. Perdew and Y. Wang, Phys. Rev. B **45**, 13244 (1992).
[24] J. P. Perdew, K. Burke, and M. Ernzerhof, Phys. Rev. Lett. **77**, 3865 (1996).
[25] O. Janson, W. Schnelle, M. Schmidt, Y. Prots, S.-L. Drechsler, S. Filatov, and H. Rosner, New J. Phys. **11**, 113034 (2009).
[26] O. Janson, A. A. Tsirlin, M. Schmitt, and H. Rosner, Phys. Rev. B **82**, 014424 (2010).
[27] A. G. Petukhov, I. I. Mazin, L. Chioncel, and A. I. Lichtenstein, Phys. Rev. B **67**, 153106 (2003).
[28] A. A. Tsirlin, O. Janson, S. Lebernegg, and H. Rosner, Phys. Rev. B **87**, 064404 (2013).
[29] N. W. Winter, R. M. Pitzer, and D. K. Temple, J. Chem. Phys. **86**, 3549 (1987).
[30] D. Muñoz, I. de P. R. Moreira, and F. Illas, Phys. Rev. B **65**, 224521 (2002).
[31] F. Neese, ORCA version 2.9, Max Planck Institute for Bioinorganic Chemistry, Muhlheim an der Ruhr, Germany, 2011.
[32] F. Neese, in *High Resolution EPR*, edited by G. Hanson and L. Berliner, Biological Magnetic Resonance, Vol. 28 (Springer, Berlin, 2008), pp. 175–232.
[33] J. P. Perdew, M. Ernzerhof, and K. Burke, J. Chem. Phys. **105**, 9982 (1996); M. Ernzerhof and G. E. Scuseria, *ibid.* **110**, 5029 (1999).
[34] S. Todo and K. Kato, Phys. Rev. Lett. **87**, 047203 (2001).
[35] A. W. Sandvik, Phys. Rev. B **59**, R14157 (1999).
[36] A. Albuquerque, F. Alet, P. Corboz, P. Dayal, A. Feiguin, S. Fuchs, L. Gamper, E. Gull, S. Gürtler, A. Honecker, R. Igarashi, M. Körner, A. Kozhevnikov, A. Läuchli, S. R. Manmana, M. Matsumoto, I. P. McCulloch, F. Michel, R. M. Noack, G. Pawlowski, L. Pollet, T. Pruschke, U. Schollwöck, S. Todo, S. Trebst, M. Troyer, P. Werner, and S. Wessel, J. Magn. Magn. Mater. **310**, 1187 (2007).
[37] See Supplemental Material at http://link.aps.org/supplemental/10.1103/PhysRevB.87.235117 for details of the structure refinement, refined atomic positions, TGA data, and hydrogen bonds within the *bc* plane.
[38] http://www.mindat.org/min-1055.html, Clinoclase.
[39] Note that we use plain LDA and GGA instead of the DFT + U methods because strong correlations in the Cu 3d shell should not affect the O-H bonds and the positions of hydrogen.

[40]S. Lebernegg, O. Janson, A. A. Tsirlin, and H. Rosner (unpublished).

[41]LSDA + U calculations arrive at the band gap of about 2.6 eV, in reasonable agreement with the blue color of clinoclase.

[42]E. Ruiz, P. Alemany, S. Alvarez, and J. Cano, Inorg. Chem. **36**, 3683 (1997).

[43]S. Lebernegg, M. Schmitt, A. A. Tsirlin, O. Janson, and H. Rosner, Phys. Rev. B **87**, 155111 (2013).

[44]M. Braden, G. Wilkendorf, J. Lorenzana, M. Aïn, G. J. McIntyre, M. Behruzi, G. Heger, G. Dhalenne, and A. Revcolevschi, Phys. Rev. B **54**, 1105 (1996).

[45]A. Oosawa, T. Kato, H. Tanaka, K. Kakurai, M. Müller, and H.-J. Mikeska, Phys. Rev. B **65**, 094426 (2002).

[46]S. Miyahara and K. Ueda, J. Phys. Condens. Matter **15**, R327 (2003); M. Takigawa, T. Waki, M. Horvatić, and C. Berthier, J. Phys. Soc. Jpn. **79**, 011005 (2010).

[47]W. Geertsma and D. Khomskii, Phys. Rev. B **54**, 3011 (1996).

[48]Y. C. Arango, E. Vavilova, M. Abdel-Hafiez, O. Janson, A. A. Tsirlin, H. Rosner, S.-L. Drechsler, M. Weil, G. Nénert, R. Klingeler, O. Volkova, A. Vasiliev, V. Kataev, and B. Büchner, Phys. Rev. B **84**, 134430 (2011).

[49]M. D. Johannes, J. Richter, S.-L. Drechsler, and H. Rosner, Phys. Rev. B **74**, 174435 (2006).

[50]R. Nath, D. Kasinathan, H. Rosner, M. Baenitz, and C. Geibel, Phys. Rev. B **77**, 134451 (2008).

[51]S. Lebernegg, A. A. Tsirlin, O. Janson, R. Nath, J. Sichelschmidt, Y. Skourski, G. Amthauer, and H. Rosner, Phys. Rev. B **84**, 174436 (2011).

[52]M. E. Zhitomirsky and A. L. Chernyshev, Rev. Mod. Phys. **85**, 219 (2013).

[53]T. Yamauchi, Y. Narumi, J. Kikuchi, Y. Ueda, K. Tatani, T. C. Kobayashi, K. Kindo, and K. Motoya, Phys. Rev. Lett. **83**, 3729 (1999); J. Kikuchi, K. Motoya, T. Yamauchi, and Y. Ueda, Phys. Rev. B **60**, 6731 (1999).

[54]U. Kuhlmann, C. Thomsen, A. V. Prokofiev, F. Büllesfeld, E. Uhrig, and W. Assmus, Phys. Rev. B **62**, 12262 (2000).

[55]D. C. Johnston, T. Saito, M. Azuma, M. Takano, T. Yamauchi, and Y. Ueda, Phys. Rev. B **64**, 134403 (2001).